Journal of Volcanology and Geothermal Research 302 (2015) 150–162

Contents lists available at ScienceDirect

Journal of Volcanology and Geothermal Research

journal homepage: www.elsevier.com/locate/jvolgeores

Experimental constraints on phreatic eruption processes at Whakaari (White Island volcano)

Klaus Mayer [a,*], Bettina Scheu [a], H. Albert Gilg [b], Michael J. Heap [c], Ben M. Kennedy [d], Yan Lavallée [a,e], Mark Letham-Brake [d,f], Donald B. Dingwell [a]

[a] Department of Earth and Environmental Sciences, Ludwig-Maximilians-Universität München (LMU), Theresienstrasse 41/III, 80333 Munich, Germany
[b] Lehrstuhl für Ingenieurgeologie, Technische Universität München, Arcisstrasse 21, 80333 Munich, Germany
[c] Laboratoire de Déformation des Roches, Équipe de Géophysique Expérimentale, Institut de Physique de Globe de Strasbourg (UMR 7516 CNRS, Université de Strasbourg/EOST), 5 rue René Descartes, 67084 Strasbourg cedex, France
[d] Geological Sciences, University of Canterbury, Private Bag 4800, 8140 Christchurch, New Zealand
[e] Earth, Ocean and Ecological Sciences, University of Liverpool, Liverpool L69 3GP, United Kingdom
[f] Kakapo Disaster Resilience Trust, 2/48 Brockworth Place, Riccarton, Christchurch 8011, New Zealand

ARTICLE INFO

Article history:
Received 21 January 2015
Accepted 20 June 2015
Available online 3 July 2015

Keywords:
Fragmentation
Hydrothermal alteration
Alunite
Rock strength
Steam flashing
Volcanic ash

ABSTRACT

Vigorous hydrothermal activity interspersed by sequences of phreatic and phreatomagmatic eruptions occur at Whakaari (White Island volcano), New Zealand. Here, we investigate the influence of sample type (hydrothermally altered cemented ash tuffs and unconsolidated ash/lapilli) and fragmentation mechanism (steam flashing versus gas expansion) on fragmentation and ejection velocities as well as on particle-size and shape. Our rapid decompression experiments show that fragmentation and ejection speeds of two ash tuffs, cemented by alunite and amorphous opal, increase with increasing porosity and that both are significantly enhanced in the presence of steam flashing. Ejection speeds of unconsolidated samples are higher than ejection speeds of cemented tuffs, as less energy is consumed by fragmentation. Fragmentation dominated by steam flashing results in increased fragmentation energy and a higher proportion of fine particles. Particle shape analyses before and after fragmentation reveal that both steam flashing and pure gas expansion produce platy or bladed particles from fracturing parallel to the decompression front. Neither fragmentation mechanisms nor sample type show a significant influence on the shape. Our results emphasize that, under identical pressure and temperature conditions, eruptions accompanied by the process of liquid water flashing to steam are significantly more violent than those driven simply by gas expansion. Therefore, phase changes during decompression and cementation are both important considerations for hazard assessment and modeling of eruptions in hydrothermally active environments.

1. Introduction

Phreatic eruptions are one of the Earth's most common, diverse and unpredictable types of eruption. They typically present a significant proximal hazard (e.g. Breard et al., 2014; Fitzgerald et al., 2014). Phreatic eruptions disintegrate and eject rock by the expansion of water as liquid, gas, or super-critical fluid (Morgan et al., 2009). Even though the ejecta contain no juvenile magma, magma at depth is nevertheless the heat source that provides the energy for the eruption. Expansion is triggered either by rapid decompression or by the heating of the system (Buttinelli et al., 2011). The pre-eruptive monitoring signals, typically associated with eruptions that yield juvenile material, may be wholly absent for phreatic eruptions (Hurst et al., 2014). At Whakaari also known as White Island volcano, New Zealand (Fig. 1), phreatic eruptions are associated with an increasing number of 1–5 Hz harmonic tremors (e.g., Nishi et al., 1996; Sherburn et al., 1998) and recent analysis has linked these events to progressive fracturing and fluid flow within the system (Chardot et al., 2015; Heap et al., 2015). Phreatic eruption dynamics vary between different hydrothermal systems, including individual eruption type from the same system and may not always follow the same patterns (Mastin, 1995; Foote et al., 2011). Phreatomagmatic processes have been investigated for over two decades using molten fuel–coolant interactions (e.g., Zimanowski et al., 1991), yet phreatic phenomena have been largely overlooked (cf. Scheu et al., 2011) in the relatively young field of experimental volcanology.

Crucial for all eruptions is decompression accompanied with the expansion of a fluid ascending to the surface. The favored model for eruptions within a hydrothermal system involves pressure build-up below a low-permeability cap rock, which fails once the pore fluid pressure exceeds the sum of lithostatic pressure and rock tensile strength (Browne and Lawless, 2001). This process may involve the flashing of water,

* Corresponding author.
E-mail address: klaus.mayer@min.uni-muenchen.de (K. Mayer).

http://dx.doi.org/10.1016/j.jvolgeores.2015.06.014

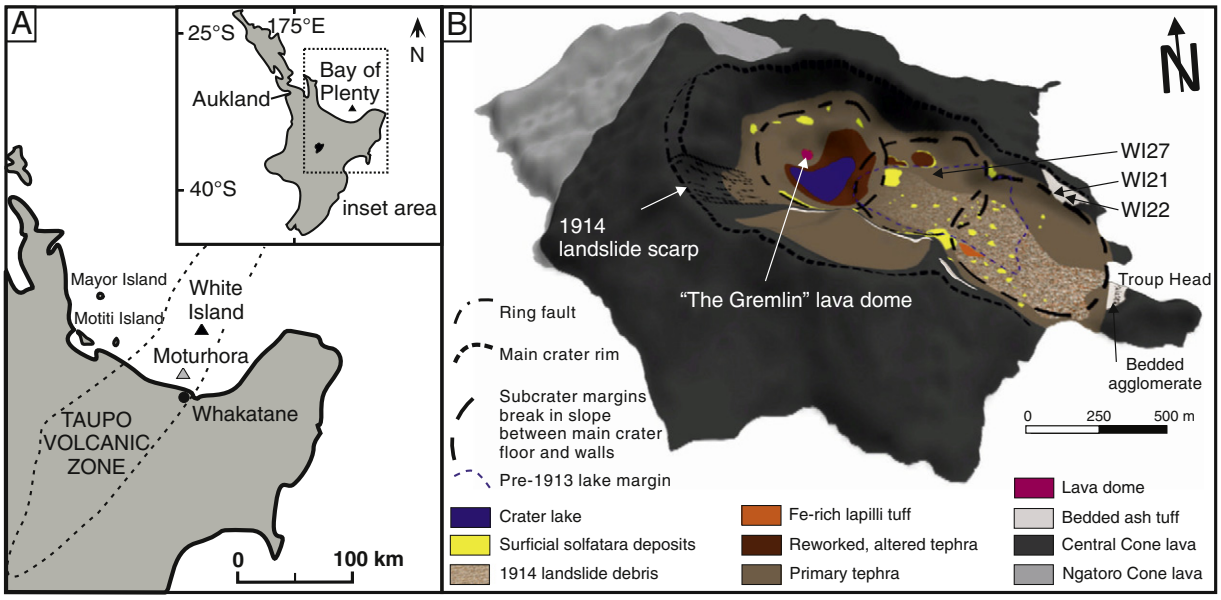

Fig. 1. (A) Location map of Whakaari (White Island volcano) approximately 50 km offshore in the Bay of Plenty within the Taupo Volcanic Zone. The inset shows a map of the North Island of New Zealand (modified from Moon et al., 2009). (B) Geological map of Whakaari showing in detail the distribution of unconsolidated crater fill (modified from Letham-Brake, 2013) and sampling sites for this study.

nearing boiling conditions, to steam and concomitant expansion due to a sudden depressurization event (Browne and Lawless, 2001). Phreatic eruptions occur over a wide range of pressure and temperature conditions and, thus, the system perturbations that give rise to phreatic eruptions may be triggered in multiple ways. Phreatic eruptions involving a reduction in the lithostatic pressure include dome collapses, landslides, and crater-lake drainages, whereas those involving an increase in temperature accompanying pressurization include adjacent magmatic intrusion and rapid magma ascent (Foote et al., 2011). Furthermore, anthropogenic interventions, such as geothermal drillings, may potentially lead to decompression events that trigger the sudden expansion of fluid within these porous media. As observed at Whakaari and many other volcanoes, phreatic eruptions can also serve as an opening phase of a later phreatomagmatic and/or magmatic eruption phreatic events (28 phreatic eruptions since 1826) exhibited at Whakaari (Fig. 2), the risk associated with the high number of tourists (>13,500 annual visitors; Letham-Brake, 2013) visiting Whakaari on a daily basis, and the relatively detailed knowledge of rock mechanics available (Moon et al., 2005; Heap et al., 2015) make Whakaari an exemplary case study for a detailed experimental investigation of phreatic processes.

A detailed survey of the literature revealed that >30 phreatic and phreatomagmatic eruptions (Fig. 2) have been recorded at Whakaari since 1826 (Letham-Brake, 2013). The recent eruptive event of 5th August 2012, associated with phreatic eruptions, led to the formation of a spiny lava dome in the crater (Global Volcanism Program, 2014). Past studies at Whakaari have focused on the surveillance and the prediction of future eruptive activity via monitoring of seismicity (Nishi et al., 1996; Sherburn et al., 1998; Jolly et al., 2012) and ground deformation (Clark and Otway, 1982; Fournier and Chardot, 2012; Peltier et al., 2009) as well as the emission (Werner et al., 2008; Bloomberg et al., 2014) and characterization of gases and fluids (Giggenbach et al., 2003). Furthermore, studies of the petrology (Graham and Cole, 1991), the origin and storage of magma (Cole et al., 2000), and the geotechnical characterization and geomorphic development of the edifice have been conducted (Moon et al., 2005, 2009; Heap et al., 2015).

Despite the abundance of previous phreatic eruptions at Whakaari and the preservation of deposits (e.g., Wood and Browne, 1996), no adequate constraints on the explosive parameters and mechanisms exist. Although the geological setting and hydrothermal system are relatively well-constrained, their interplay in general, as well as in view of the mechanisms triggering phreatic eruptions, is not yet fully understood. Adding to this complexity is the fact that the physical properties and mechanical behavior of Whakaari rocks are highly altered due to the activity of the hydrothermal system (Pola et al., 2013; Wyering et al., 2014; Heap et al., 2015). Changes in state of alteration during thermal stressing, as is the case during shallow (~500 m below sea level) magma intrusion, commonly induce mineral breakdown, which leaves a skeletal porous rock with deteriorated mechanical strength (Peltier et al., 2009; Heap et al., 2012).

The porosity of a rock controls the amount of gas stored and therefore the energy available for release during fragmentation for a given decompression step (Spieler et al., 2004; Alatorre-Ibargüengoitia et al., 2010). Earlier studies have defined the fragmentation threshold (the minimum pore pressure differential required to fully fragment the sample) as being inversely proportional to the porosity (Spieler et al., 2004). Foote et al. (2011) and Rager et al. (2013) have presented results of experimental phreatic fragmentation induced by both inert gas overpressure and steam flashing in vesicular rocks, and made an initial evaluation of the influence of pressure, sample alteration and sample saturation on these processes. Here, we present the results of a systematic experimental campaign employing a shock-tube apparatus (Aldibirov and Dingwell, 1996a) to perform decompression experiments on both hydrothermally altered consolidated and loose deposits, inferred to reflect those deposits existing at depth at Whakaari (Heap et al., 2015). Specifically, we have investigated the influence of sample type and fragmentation mechanism (steam flashing versus gas expansion) on grain size and shape and on fragmentation and ejection velocities.

2. Geological setting

Whakaari is New Zealand's most active volcano and is characterized primarily by phreatic and phreatomagmatic eruptions, interspersed by occasional strombolian events (Cole and Nairn, 1975; Simkin and Siebert, 1994). Located 50 km offshore from the North Island of New Zealand (Fig. 1), this andesitic–dacitic, stratovolcano exhibits strong fumarolic activity and outgassing (Bloomberg et al., 2014) interspersed by eruptive events. Whakaari is the northernmost active volcano within the Taupo Volcanic Zone (TVZ), which is itself a 250-km-long belt of mainly rhyolitic and andesitic, Quaternary to present volcanism

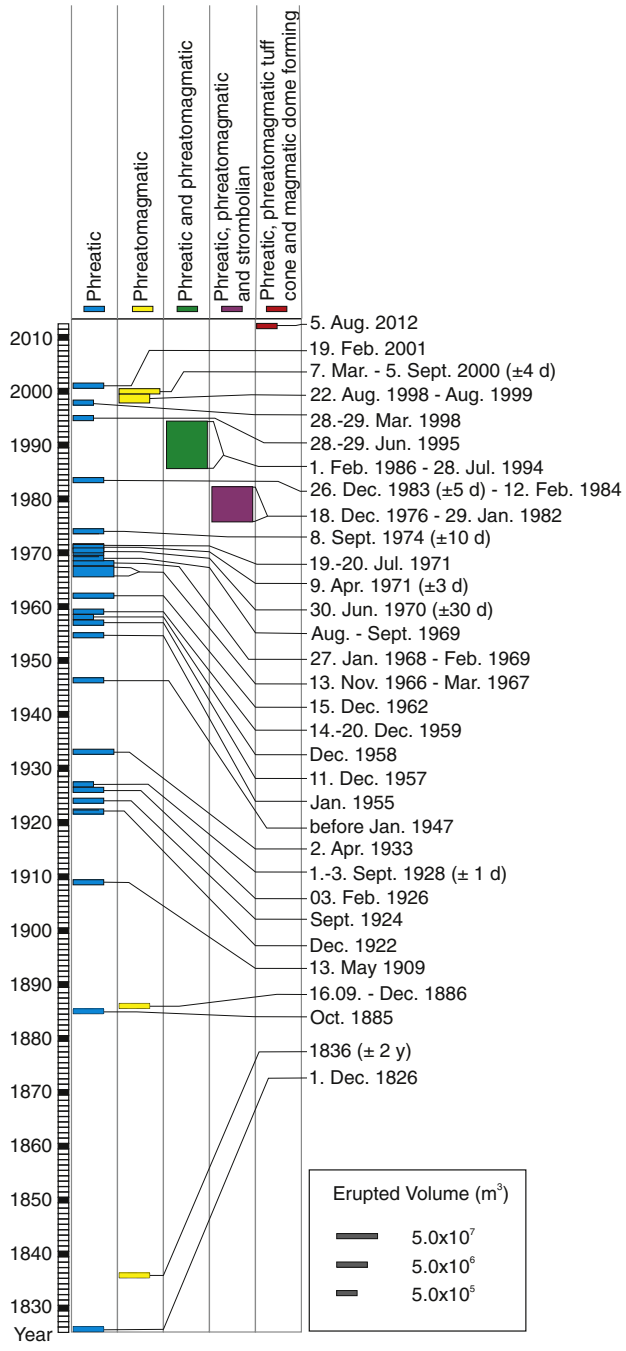

Fig. 2. Timeline of historic eruptions at Whakaari from 1826 to 2012. Single events as well as periods of activity are classified based on the dominant activity reported in literature. A table (modified after Letham-Brake, 2013) listing the events as well as the used literature can be found in the Supplementary material. Type of eruption and estimated erupted volume are indicated in the figure.

(Black, 1970). The northeast–southwest-trending TVZ extends 200–270 km west of the trench resulting from the convergence of the Pacific and Australian plates (Nishi et al., 1996).

The island occupies an area of approximately 3.3 km^2 with a maximum elevation of 321 m above sea level and represents the emergent summit of the much larger White Island Massif (Nishi et al., 1996) whose basal extent of 16 km × 18 km yields a total volume of ~78 km^3 (Duncan, 1970; Cole et al., 2000). The edifice consists of two overlapping composite cones, comprised of major lava flow units, and minor tuff and tephra units. The older Ngatoro cone only outcrops in the west, whereas the younger and active central cone forms most of the island (Black, 1970; Duncan, 1970; Cole and Nairn, 1975; Cole et al., 2000). The NW–SE elongated main crater (1.2 km × 0.4 km) is a complex of three coalesced prehistoric subcraters, infilled with unlithified deposits from historical eruptions, which have been confined to the western subcrater and the western half of the central subcrater (Houghton and Nairn, 1989a, 1991). Due to the occurrence of a large (210×10^6 m^3) prehistoric, eastward-trending sector collapse (Moon et al., 2009), the horseshoe-shaped, flat-floored crater is breached to the sea in three locations in the southeast (Cole et al., 2000). The collapse of the main crater wall in the southeast caused a debris avalanche of 2.5×10^5 m^3, which has covered parts of the main crater floor (Ward, 1922; Bartrum, 1926 in. Hamilton and Baumgart, 1959).

Magma has been hypothesized to exist transiently at shallow depths (<500 m) as well as extending to deeper chambers at 1–2 km and 2–7 km (Cole et al., 2000; Houghton and Nairn, 1989a in: Werner et al., 2008). This most shallow magma is believed to be the source for large ground deformation and seismicity episodes and, ultimately, the large acidic, volcano–hydrothermal system (Giggenbach, 1987).

2.1. Hydrothermal setting

Fumarole and spring discharge analyses have indicated that the hydrothermal system of Whakaari has been active for more than 10,000 years (Giggenbach and Glasby, 1977; Giggenbach et al., 2003). Hot fluids released from the magma condense in contact with meteoric groundwater and circulate within the conduit-hosted, volcano–hydrothermal system that has been interpreted to occur in isolated, chemically-sealed zones around the volcano (Giggenbach, 1987). More recent isotopic studies show that, there is less seawater component in the fumarolic output of the western and central subcraters than the eastern subcrater (Giggenbach et al., 2003; Bloomberg et al., 2014).

The hydrothermal system finds its expression in the form of numerous fumaroles, steaming ground areas, hot springs, and a crater lake. Fumarole temperatures vary between 100 and 800 °C in response to outgassing fluctuations of the magma, yielding cooling and heating stages (Giggenbach et al., 2003). These fluctuations further correlate with variations in the discharge of fluids (H_2O, CO_2, HCl) (Pirajno, 2009). The low pH of the crater lake (1.2–2.4) (Werner et al., 2008), the acid springs (0.7–1.4), and the pools (0.7–0.8) as well as the strong H^+ activity of the hydrothermal system results from ingress of HCl and H_2S, which are the dominant acids in the fluids (Giggenbach et al., 2003; Pirajno, 2009). These acidic fluids promote mineral dissolution and corrosion leading to substructure weakening and an increased susceptibility for further alteration (Houghton and Nairn, 1989a, 1991).

Geophysical evidence suggests that the hydrothermal fluid flow is focused primarily in the thermally weakened zones, such as proximity of former and newly-formed eruption craters as well as in the 200–650 °C fumarole fields (Clark and Otway, 1982; Christoffel, 1989; Hurst et al., 2004; Peltier et al., 2009; Fournier and Chardot, 2012). The semi-regular cycling (2–10 yr) of the hydrothermal fluid flow causes a cycling in ground inflation (≤250 mm) due to increases in pore pressure as well as to thermal expansion of the reservoir rocks at depths of ~200–600 m, both interpreted as evidence of the presence of magma below the central and western subcraters (Peltier et al., 2009; Fournier and Chardot, 2012).

2.2. Eruption history

At Whakaari, the interplay of hydrological factors and magmatic activity helps determine the nature of hydrothermal processes and the characteristics of associated eruptions (Houghton and Nairn, 1991). A prehistoric sector collapse (<3.4 ka) may have induced a fundamental change in the hydrothermal fluid flow field by eradicating low permeability cone lavas and thereby allowing the infiltration of meteoric water (Letham-Brake, 2013). This may, in turn, have favored the change

from at least 19 prehistoric, magmatic lava-flow producing eruptions (Cole et al., 2000) to long periods of continuous fumarolic and hydrothermal activities interspersed by a minimum of 32 small (VEI 1–3) phreatic and phreatomagmatic eruptions recorded since 1826. The main crater-forming eruptions occurred in 1933, 1947, 1965–1966, 1968, 1971, 1976–1982 and 1986–1991. The long, 1976–1982 period of unrest was characterized by strombolian and phreatomagmatic eruptions (Clark and Otway, 1982; Houghton and Nairn, 1989b, 1991). All historic activities have occurred within the western subcrater and the western part of the central subcrater (Houghton and Nairn, 1991).

3. Sample characterization

This study focuses on three volcaniclastic rocks from lithostratigraphic units at Whakaari. Two consolidated ash tuff units (WI21, WI22) were collected from the scree at the foot of the eastern crater wall (Fig. 1B), estimated to originate from approximately 70 m beneath the current cliff top (Heap et al., 2015). One recent, unconsolidated tephra (WI27) typical of the main crater fill deposit has been sampled at 1-m depth within the central subcrater (Fig. 1B). X-ray fluorescence analysis (XRF) of the bulk geochemical composition of each sample was conducted using a Philips Analytical Magix Pro WDX-spectrometer at the Ludwig-Maximilians-Universität München (LMU). Results of analyses on pressed powder tablets are presented in Table 1. Mineralogical analysis of the samples was carried out using X-ray powder diffraction analysis (XRD) conducted at the Technische Universität München (Table 2). For XRD analysis, the samples were disaggregated, mixed with an internal standard (10% ZnO), and ground for 8 min with 10 ml of isopropyl alcohol in a McCrone Micronising Mill using agate cylinder elements. The powder mounts of the samples were analyzed with a Philips PW 1800 X-ray diffractometer (CuKα, graphite monochromator, 10 mm automatic divergence slit, step-scan 0.02° 2θ increments per second, counting time 1 s per increment, 40 mA, 40 kV). Quantification of the crystalline and amorphous phases in the whole rock powders was performed by using the Rietveld program BGMN (Bergmann et al., 1998).

A comparison of chemical compositions measured by XRF with those calculated based on XRD results and the chemical composition of the involved phases allowed us to distinguish if the amorphous phase was predominantly opal-A or volcanic glass.

The ash tuffs (WI21 and WI22) consist of altered crystal fragments and devitrified glass shards (Figs. 3–4), which are composed primarily of hydrated amorphous silica (opal-A). Alunite and minor opal-A cement the crystal-vitric ash tuffs (Fig. 4) in which the original shards and crystal fragments are hard to distinguish from one another due to massive opalization. The maximum particle sizes of the ash tuffs are on the order of 0.2 mm (WI21) and 0.3 mm (WI22) and the dominant pore size diameters are on the order of several hundred microns (Figs. 3–4). The white/gray ash tuff (WI21) consists of amorphous phases, predominantly opal-A (66%), alunite (32%) and minor amounts of gypsum, cristobalite and quartz (Table 2). The gray, ash tuff (WI22) is more heterogeneous, showing a distinct bedding of approximately 10 mm-thick layers of low and high porosities. XRD analysis and chemical data show that it is mainly composed of opal-A (90%), alunite (6%), cristobalite (3%), and minor quantities of gypsum and quartz (Table 2). The brown, unconsolidated, poorly-sorted primary tephra (Fig. 3) comprising 80% coarse ash and 20% lapilli (hereafter referred to as "ash/lapilli") is composed of amorphous volcanic glass (59%), plagioclase (15%), pyroxene (9%), alunite (8%), and minor quantities of gypsum and cristobalite.

Table 1
Average bulk geochemical composition of studied samples based on X-ray fluorescence analyses.

Sample	WI21	WI22	WI27
SiO_2	59.70	79.60	62.67
Fe_2O_3	0.90	1.65	6.84
Al_2O_3	13.14	7.03	12.84
MnO	0.01	0.01	0.07
CaO	0.71	0.85	3.94
MgO	0.06	0.32	2.65
K_2O	3.37	1.07	2.11
Na_2O	1.57	0.48	1.28
TiO_2	1.19	1.06	0.70
P_2O_5	0.10	0.05	0.09
LOI	18.46	7.79	6.36
Sum	99.21	99.91	99.55

Table 2
Mineral composition of studied samples based on X-ray diffraction analyses.

Sample	WI21	WI22	WI27
Amorphous phases			
Opal-A	66 ± 6	90 ± 3	
Volcanic glass			59 ± 5
Plagioclase			15 ± 2
Pyroxene[a]			9 ± 2
Alunite[b]	32 ± 3	6 ± 3	8 ± 2
Gypsum	1 ± 0.5	1 ± 0.5	2 ± 1
Cristobalite	1 ± 0.5	3 ± 1	7 ± 1
Quartz	<1	<1	
Sum	100	100	100

[a] Includes ortho- and clinopyroxene.
[b] Includes Na- and K-dominated alunites.

4. Experimental methods

Rapid decompression experiments were performed using a "fragmentation bomb" apparatus (Alidibirov and Dingwell, 1996a,b; Martel et al., 2000; Spieler et al., 2003, 2004; Mueller et al., 2005, 2008; Kueppers et al., 2006; Scheu et al., 2006, 2008; Rager et al., 2013; Richard et al., 2013). The device in its present configuration permits the accurate control of temperature, gas overpressure and decompression rate in order to best represent variable volcanic and hydrothermal conditions. It is, in essence, a shock-tube apparatus, consisting of a stainless steel low-pressure tank (l = 3.0 m; d = 0.4 m) at ambient pressure and temperature to collect the experimentally generated pyroclasts, and a high-temperature steel autoclave in which the sample is mounted (Fig. 5). The sample (either dry or water saturated) is inserted in the autoclave (l = 450 mm; d = 25 mm), which is externally heated up to 400 °C and pressurized up to 25 MPa using argon gas; when the sample is water saturated, water turns into a supercritical fluid. The pressure and temperature in the system are monitored at rates of 1000 Hz and 2 Hz, respectively. A dynamic pressure sensor and a thermocouple are located at the bottom of the sample; the second pressure sensor sits at the upper end of the autoclave, 225 mm above the sample (Fig. 5). The autoclave and low-pressure tank are separated by a set of two diaphragms that enable triggering of decompression by a controlled failure of the uppermost diaphragm. The rupture leads to instantaneous failure of the other diaphragm, and rapid decompression of the high-pressure autoclave. Upon diaphragm failure, a shock wave travels upwards into the low-pressure collector tank and a rarefaction wave propagates downwards into the autoclave traveling through the sample. The sample fragments in a brittle manner in a layer-by-layer fashion (Aldibirov and Dingwell, 2000; Fowler et al., 2010) and the particles are ejected into and stored in the collector tank.

All three sample series experiments were conducted on both dry and fully water-saturated samples. For consolidated samples (WI21, WI22) cylindrical samples, 25 mm in diameter and 60 mm in length, were cored, ground flat and parallel. All cylinders as well as the loose ash/lapilli samples were dried in an oven at 65 °C for at least 24 h until fully dry. Prior to the rapid decompression experiments, porosity and bulk density of each sample were determined using a helium pycnometer (Ultrapyc 1200e®, Quantachrome, USA); the results are in good agreement with the triple-weight water saturation technique

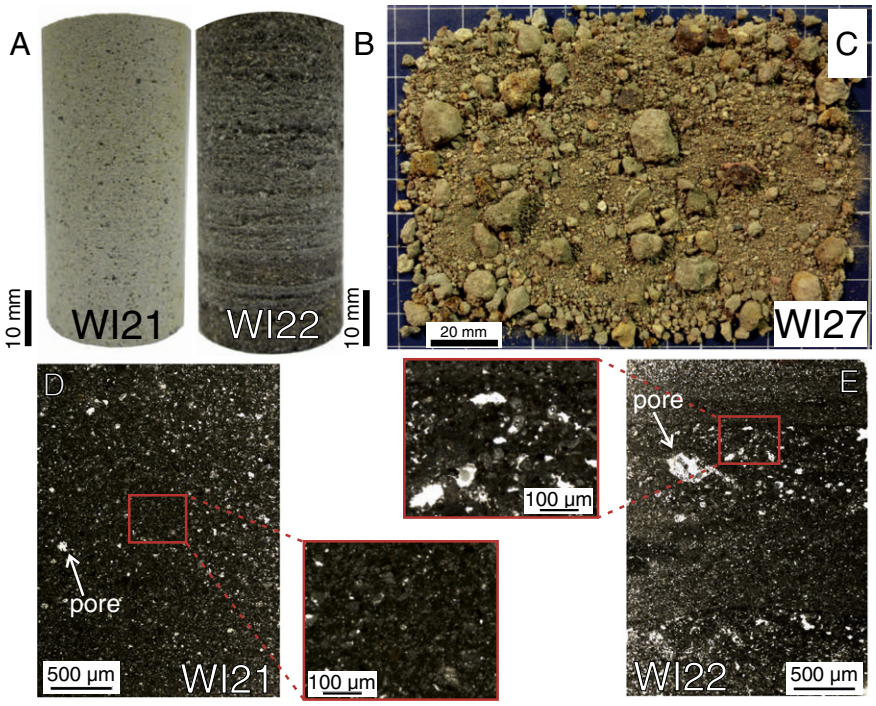

Fig. 3. Photographs and thin section scan images of the Whakaari ash tuff WI21 (A and D), WI22 (B and E) and the loose ash/lapilli sample WI27 (C). The insets show close-up images of the samples. WI22 samples are less homogenous and contain larger pores; the distribution of fine and coarse particles generates a clearly visible layering of the sample.

(Table 3; Heap et al., in, 2015). The two ash tuff samples (WI21, WI22) used for fragmentation experiments have mean porosities of 32 and 49%, respectively, whereas the loose ash/lapilli (WI27) has a porosity of 51% (Table 3). Gas permeability of selected samples was determined using a benchtop (argon) permeameter. For the ash tuffs WI21 and WI22, permeability was measured under a confining pressure of 1 MPa and was found to be 1.5×10^{-16} and 3.5×10^{-14} m^2 respectively (Table 3). For the loose ash/lapilli (WI27), we poured material (excluding the lapilli larger than about 5 mm) into a rubber jacket (20 mm in diameter and about 40 mm length) and measured its permeability under a confining pressure of 0.3 MPa. The permeability of WI27 was measured to be 3.4×10^{-12} m^2 (Table 3). For rapid decompression experiments the samples were mounted into a steel sample holder and directly placed inside the autoclave ready for dry fragmentation experiments. For experiments in the presence of steam flashing, samples (already mounted into a sample holder) were submerged in water and placed under a vacuum for at least 72 h to facilitate water to be absorbed into the connected porosity assuring maximum water saturation. By contrast, unconsolidated samples were poured into sample holders with effort made to ensure that their particle size distribution was not misrepresented (i.e., undisturbed from laboratory manipulation and water-saturated in the same manner).

The fragmentation threshold was first determined for both ash tuff sample series at room temperature (dry condition); for this purpose, a series of tests was done where the applied pore pressure was successively increased (from 2 MPa) until complete fragmentation of the samples was achieved. In cases where the sample did not fragment, the same sample was tested again with the initial pressure raised by an increment of 0.5 MPa. This procedure was continued until the removal of a few millimeters of the sample surface occurred. This fragmentation

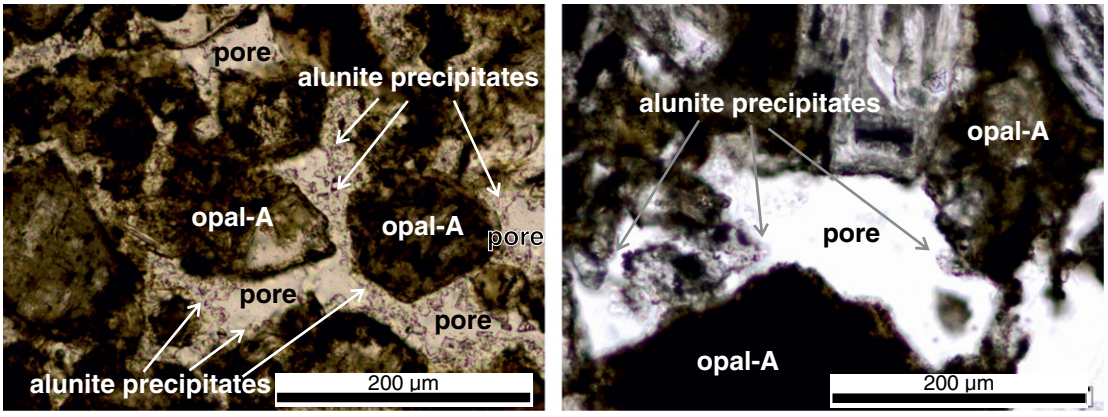

Fig. 4. Photomicrographs (taken under transmitted cross-polarized light) show amorphous opal particles cemented by alunite. Alunite precipitated within the pores, on opal particles. (A) WI21 shows smaller pores with a higher amount of alunite precipitates compared with (B) showing WI22. Main components of pores, alunite precipitates, and opal-A are identified on the figures.

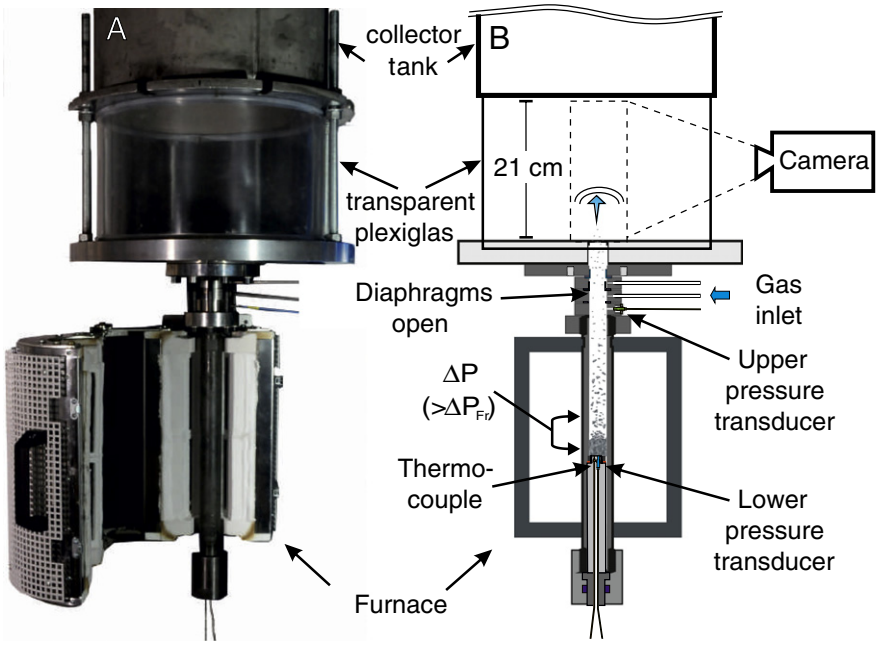

Fig. 5. Photograph (A) and schematic drawing (B) of the experimental setup used during this study. The high pressure autoclave is separated from the low pressure tank by a set of two diaphragms. Pressure and temperature within the autoclave are monitored by transducers and a thermocouple (adapted from Scheu et al., 2006). Particles fragmented during decompression are ejected into the ambient pressure collector tank. Particle ejection is monitored by a high speed camera through a transparent plexiglass.

initiation is usually 0.5–1.5 MPa below the complete fragmentation of the sample, which is defined as the fragmentation threshold (Scheu et al., 2006).

Giggenbach et al. (2003) estimates the temperatures in the proximity of the fumaroles, within the uppermost 200 m below the western subcrater, in the range from 200 to 300 °C (Fig. 6). In order to compare fragmentation initiated by steam flashing following rapid decompression, with fragmentation initiated by argon gas expansion, both water-saturated and dry samples were heated to 270 °C and pressurized to 6.5 MPa. The temperature was chosen in agreement to the temperatures estimated by Giggenbach et al. (2003); the applied pressure was fixed to 6.5 MPa in order to allow decompression from the liquid phase slightly above the boiling curve but still at a reasonable pressure condition for Whakaari. For a precise acquisition of the dwell condition for the experiments performed on dry samples, samples were initially pressurized to about 4 MPa. The target temperature of 270 °C was reached after a heating time of 45 min whereas during the last stage of heating, the remaining pressurization required for a dwell pressure of 6.5 MPa was applied. Holding these final conditions for a dwell time of 10 min ensured temperature and pressure equilibrations over the entire sample before triggering the fragmentation.

For the experiments performed on water-saturated samples, the autoclave was first pressurized with argon gas to 4.0 MPa before heating (Fig. 7), thereby holding the water in the liquid state throughout the experiments. Shortly before approaching the final temperature of 270 °C, the autoclave was pressurized further with argon to the target dwell conditions. The final dwell condition was held constant for a further 10 min to ensure equilibrated conditions within the autoclave and the sample, before the controlled opening of the diaphragms was initiated. During the decompression of the system, the phase transition from liquid water to water vapor is crossed (Fig. 7).

Following a test, the analysis of the pressure decay monitored by the dynamic pressure transducers, located above and below the sample, provides a quantification of the fragmentation speed for consolidated samples or unloading speed for unconsolidated samples (e.g. Alatorre-Ibargüengoitia et al., 2010 and references therein). For the time assessment of pressure decay though a sample, the travel time of the rarefaction wave from the upper pressure sensor to the top of the sample was derived according to the procedures developed by Scheu et al. (2006).

The ejection of the gas–particle mixture was imaged by a high-speed camera (Phantom V710®, Vision Research, USA). The entire ejection was monitored at 10,000 frames per second at an area (h = 21.0 cm, w = 12.5 cm) at the base of the collector tank, just above the diaphragms (Fig. 5). This allows the tracking of fragmented particles and an estimation of their ejection velocities.

To investigate the grain size of fine particles, the experimentally generated pyroclasts of all experiments were collected from the low-pressure tank. By dry sieving the particles of >63 μm at half-phi steps, the particle-size distribution was evaluated. In addition, for WI21 and WI22, the long (L), intermediate (I) and short (S) axes of each fragment from phi sizes −2.5 (5.6 mm) to −1.5 (2.8 mm) were measured. These particles were large enough to be measured with calipers and were present in the products of all experiments. The S/L ratio and [(L–I)/(L–S)] form index developed by Sneed and Folk (1958) was

Table 3
Summary of the rock physical properties of investigated samples. Porosity measurements from Heap et al. (2015) by using the triple-weight water saturation technique and permeability of the ash/lapilli at a confining pressure of 0.3 MPa are also included. Permeability measurements of WI21 and WI22 were collected under a confining pressure of 1 MPa. Note: Given values for density and porosity are averaged on all samples and might therefore differ from values shown in figures.

Sample	Density (g/cm^3)	Porosity (connected) (%)	Porosity (closed) (%)	Porosity Heap et al.(2015) (%)	Gas permeability (m^2)
WI21 ash tuff	2.3	32	3.8	29	1.9×10^{-15}
WI22 ash tuff	2.2	49	3.2	46	3.1×10^{-15}
WI27 ash/lapilli	2.5	51	3.0	n.m.	3.4×10^{-12}

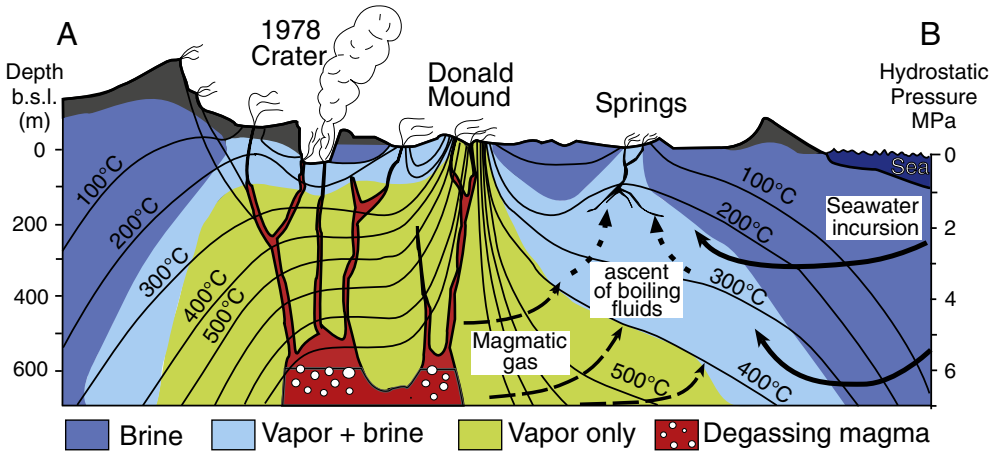

Fig. 6. Schematic cross section through Whakaari hydrothermal system. The dashed, dashed–dotted and solid arrows indicate flows of the magmatic gas, boiling brines and seawater, respectively (modified after Giggenbach et al., 2003). The subsurface of the highly active stratovolcano is characterized by regimes of liquid and gaseous fluids.

employed to determine the grain shape for each fragment. We calculated the average and standard deviation of the S/L ratio and the [(L–I)/(L–S)] form index and plotted them for the dry and water-saturated experiments for WI21 and WI22.

5. Results

5.1. Fragmentation threshold

In order to account for sample heterogeneities, we repeated the determination of the fragmentation threshold three times for each ash tuff. The low porosity (Φ = 31–33%, WI21) and the high porosity (Φ = 44–47%, WI22) ash tuffs fully fragment at initial pressures ranging between 4.3–5.3 MPa and 3.8–4.0 MPa, respectively (Fig. 8). The results are fully in accordance with the fragmentation threshold defined in previous studies (e.g., Spieler et al., 2004) and therefore are also in agreement with the fragmentation criterion of Koyaguchi et al. (2008).

5.2. Fragmentation speed

Rapid decompression experiments at 270 °C and an initial applied pressure of 6.5 MPa were performed for all three sample series under both dry and water-saturated conditions in order to determine the fragmentation speed. Fig. 9A illustrates the following dependencies of the fragmentation speed: (1) for identical conditions (dry argon or steam flashing), the fragmentation speed of the consolidated ash tuffs increases with porosity. For the dry experiments, samples with ~32% porosity have fragmentation speeds between 10 and 28 m/s, and at ~52%, porosity fragmentation speeds increase to 53–83 m/s. Fragmentation speed in the presence of steam flashing increased with increasing porosity in the ash tuffs (~34% samples 75–130 m/s and ~51% samples 160–180 m/s). Within a sample series (given mean porosity), the presence of steam flashing significantly increases the speed of fragmentation. Ash tuffs where steam flashing occurred led to increased fragmentation speeds for WI21 (Φ = 33%) from 10–28 m/s to 75–130 m/s and for the highly porous tuffs WI22 (Φ = 51%) from 53–83 m/s to 160–180 m/s, respectively. (3) The unloading speed of loose ash/lapilli samples (WI27) is increased for both, dry and steam flashing conditions, compared with a consolidated ash tuff of comparable porosity (WI22). Dry ash/lapilli samples were unloaded at a speed of 167–203 m/s whereas steam flashing led to an unloading speed of 305–353 m/s (Fig. 9A).

5.3. Ejection speed of the particle front

The duration of the entire gas–particle ejection is on the order of 0.15 s to 0.25 s for the experiments with the ash tuffs and on the order of 0.10 s to 0.15 s for the ash/lapilli (Table 4). The velocity of the gas–particle mixture was measured by high-speed videography for

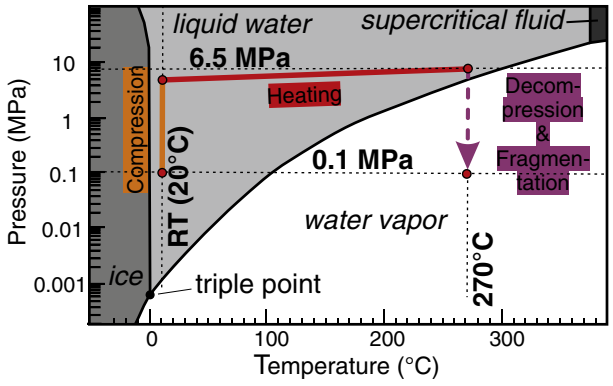

Fig. 7. Experimental pressure and temperature conditions. Both dry and water saturated samples were initially pressurized to about 4 MPa, then heated to 270 °C and further pressurized to 6.5 MPa during the last stage of heating. Water within the pores of saturated samples immediately flashes to steam during decompression when crossing the phase transition from liquid water to water vapor.

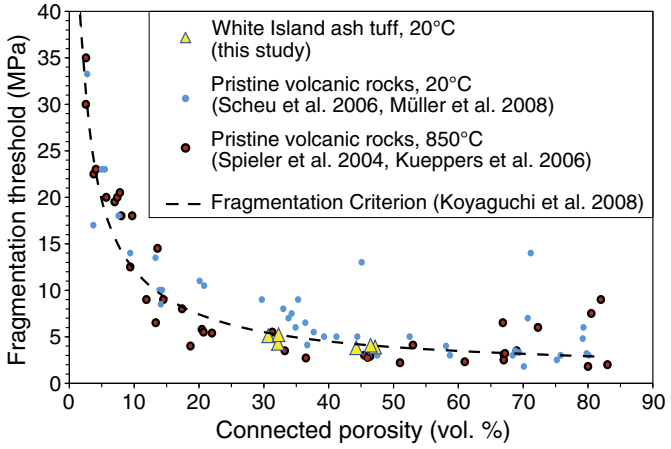

Fig. 8. Fragmentation threshold of Whakaari ash tuffs (triangles) at 20 °C during rapid decompression. Fragmentation thresholds for pristine volcanic rocks at 850 °C and 20 °C also are compiled. The dashed line corresponds to the fragmentation criterion proposed by Koyaguchi et al. (2008). Samples with a higher porosity fragment at a lower initial pore pressure. Whakaari samples confirm the criterion plotting slightly below the dashed line.

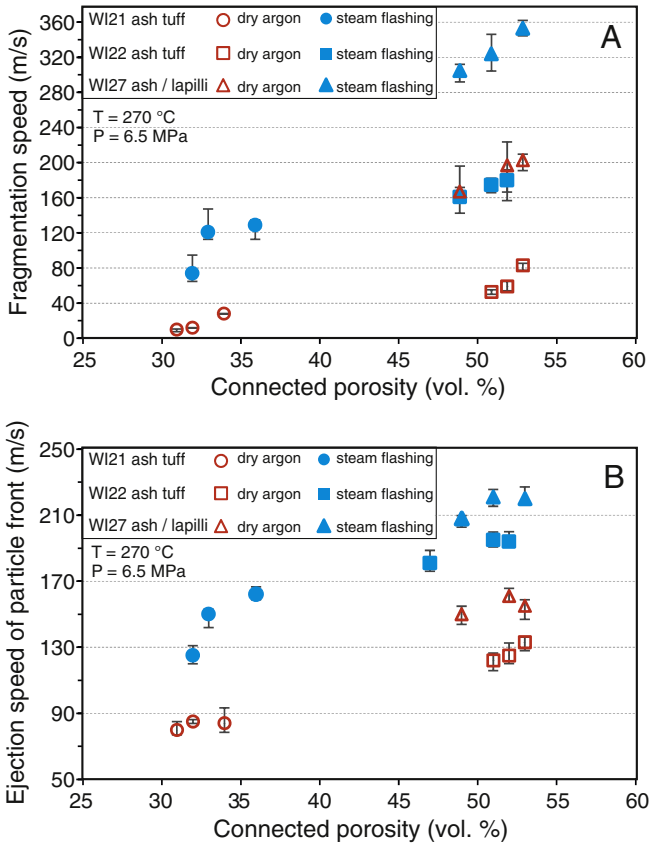

Fig. 9. Fragmentation and ejection speeds of Whakaari samples. All experiments were conducted at 270 °C and 6.5 MPa initial pressures. (A) Fragmentation speed due to dry argon gas expansion and steam flashing. Fragmentation speed increases with porosity as well as steam flashing. The speeds obtained for the ash/lapilli samples correspond to the unloading of the sample out of the autoclave, thus termed unloading speed. In these experiments, further fragmentation of the particles may occur; however, it is not necessary. (Note: The error bars indicate the uncertainties in the determination of the fragmentation onset. Errors for the dry experiments with the ash tuffs are small leading to error bars smaller than the symbols usEd.). (B) Ejection speed of the particle front in the presence of argon gas expansion and steam flashing. The ejection speed values correspond to the average of the velocities of several particles (≥5) traveling at the front of the gas–particle mixture. The ejection speed of the ash tuff increases with porosity and is lower than for the unconsolidated ash/lapilli. Steam flashing significantly enhances the ejection speed for all sample types. (Note: The error bars reflect the extrema of each data point.).

each experiment (except WI22-6). Velocities of the particles traveling at the front of the ejected plumes were estimated by considering the average of several (≥5) particle velocities (Fig. 10). The determination of the ejection speed is limited by the visibility of single particles within the plume of either argon gas and dust or steam and fine dust, respectively (Fig. 10). Therefore the maximum velocity of particles ejected in steam flashing experiments, obtained by the technique of high-speed video analysis, is an approximation to the true maximum velocity. In addition, the fastest particles, if visible at all, are hard to track in two consecutive still frames. The obtained ejection speeds of all three sample series (Table 4) are illustrated in Fig. 9B showing the following dependencies: (1) at identical conditions (dry argon or steam flashing), the ejection speed of the ash tuff particle front increases with porosity. In case of dry fragmentation from 80–85 m/s for WI21 (Φ = 32%) to 122–133 m/s for WI22 (Φ = 52%) and for fragmentation dominated by steam flashing, the ejection speed of particle front was enhanced from 125–162 m/s (Φ = 34%) to 181–195 m/s (Φ = 50%). (2) Within a sample series ejection speed is significantly increased in the presence of steam flashing. From 80–85 m/s to 125–162 m/s for WI21 and from 122–133 m/s to 181–195 m/s for WI22 respectively. (3) For both, dry argon and steam flashing conditions, the ejection speed of loose ash/lapilli samples (WI27) is higher, compared with a consolidated

Table 4
List of samples used for fragmentation experiments with experimental condition and porosity to quantify the fragmentation speed and the ejection speed of particles front. $\Delta t_{ejection}$ corresponds to the total duration (s) over which particle ejection occurs. Note: unloading speeds of WI27 samples are given under column fragmentation speeds ($V_{fragmentation}$).

Sample	Experimental condition	Porosity (%)	$V_{fragmentation}$ (m/s)	$V_{ejection\ front}$ (m/s)	$\Delta t_{ejection}$ (s)
WI21-1	Dry argon	34	28	84	0.24
WI21-2	Dry argon	32	12	85	0.25
WI21-3	Dry argon	31	10	80	0.25
WI21-4	Steam flashing	36	129	162	0.20
WI21-5	Steam flashing	32	74	125	0.22
WI21-6	Steam flashing	33	121	150	0.20
WI22-2	Dry argon	51	53	122	0.19
WI22-3	Dry argon	52	59	125	0.20
WI22-4	Dry argon	53	83	133	0.19
WI22-5	Steam flashing	47	No record	181	0.16
WI22-6	Steam flashing	49	161	No video	No video
WI22-7	Steam flashing	52	180	194	0.15
WI22-8	Steam flashing	51	174	195	0.16
WI27-1	Dry argon	53	203	155	0.14
WI27-2	Dry argon	49	167	150	0.15
WI27-3	Dry argon	52	197	161	0.14
WI27-5	Steam flashing	49	305	208	0.12
WI27-6	Steam flashing	51	324	221	0.11
WI27-7	Steam flashing	53	353	220	0.10

ash tuff of comparable porosity (WI22). Ash/lapilli samples were ejected at a speed of 150–161 m/s under dry conditions and at a speed of 208–221 m/s in the presence of steam flashing.

For both ash tuffs, the ejection velocity of the gas–particle mixture is higher than the fragmentation speed in each experiment (Fig. 9A and B). In contrast, the maximum ejection speed of the loose ash/lapilli is lower than the unloading speed.

5.4. Particle size and shape

The evaluation of the particle-size distribution of the experimentally generated pyroclasts is shown in Fig. 11. Due to the sealing between the plexiglass cylinder and the collector tank, as well as the adhesion of very fine particles on the lid and along the rim of the tank, a complete recovery of the very finest fraction was not possible; however, a minimum weight yield of 95% was achieved. WI21 ash tuffs showed a peak in the particle-size distribution at phi = −0.5 (1.5 mm) when fragmented dry with argon (Fig. 11A). The samples fragmented by steam flashing exhibit a peak at a smaller phi-value between 0 and 1 (1–0.5 mm). Dry argon fragmented WI22 samples demonstrate the highest particle fraction at phi-values between −3 and −1.5 (8–3 mm), whereas the steam-flashing experiments enhanced the generation of fine particles, shifting the peak to phi = 1 (0.5 mm) (Fig. 11B). The unconsolidated WI27 ash/lapilli particles showed grain size peaks at phi = 1 (0.5 mm). In contrast to WI21 and WI22 a grain size distribution prior to experimentation (raw) was determined for the loose ash/lapilli, which is biased by a few coarser particles leading to a peak at phi = −3 (8 mm). The shift of the grain size distribution curve from prior to post experimentation is evidence of fragmentation despite their lack of consolidation (Fig. 11C). Fragmentation dominated by steam flashing increases the proportion of fine particles.

To quantify variations in particle shape, the three axes of the generated particles from experiments on WI21 and WI22 were measured and used to plot the S/L ratio and [(L–I)/(L–S)] form index with the standard deviation (Fig. 12). In total, 134 particles with phi sizes ranging from −2.5 to −1.5 were used for the analysis of the particle shape as these phi sizes have been produced in every experiment and were measureable with a set of calipers. The shape of particles fragmented by steam flashing for sample WI21 was slightly different to particles fragmented by gas expansion, and also slightly different than any particles generated in the experiments on the sample WI22 (Fig. 12).

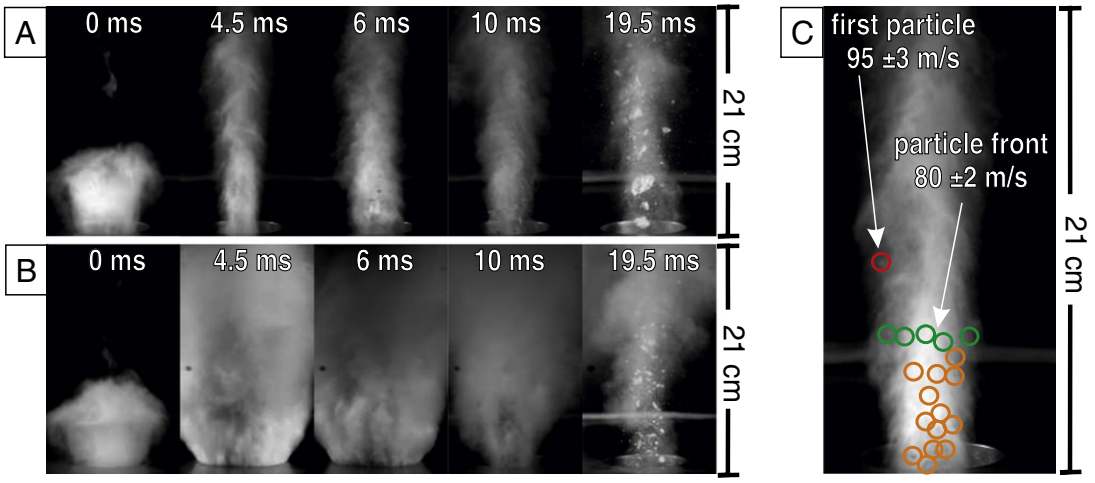

Fig. 10. Sequence of still frames from high-speed camera recordings. (A) Images showing the front of the argon gas and argon–gas–particle mixture after fragmentation of a dry WI21 sample at 6.5 MPa and 270 °C. The narrow plume of argon gas contains large particles with a diameter of up to 1.5 mm. (B) Sequence showing the front of the argon gas followed by the dense and almost opaque steam and steam–particle mixture of a saturated WI21 sample fragmented in the presence of steam flashing at 6.5 MPa and 270 °C. Note: 19.5 ms after decompression, the particles within the steam jet are significantly smaller than particles produced in the dry experiment (A). (C) Still frame showing a single particle ejected at a higher speed ahead of the particle front. Note: Tracking of first particles arriving in the field of view is partly hindered by the opacity/poor visibility caused by steam, dust, and very fine particles.

Nevertheless, the shape of the particles from the different experiments/conditions is not significantly different as the standard deviation bars of the individual samples show a significant overlap.

6. Discussion

Our results show that, under identical pressure and temperature conditions, eruptions accompanied by the process of liquid water flashing to steam are significantly more violent that those driven simply by gas expansion. Thus, steam flashing changes the conditions for and the progression of fragmentation.

6.1. Fragmentation threshold

The pressure applied during the fragmentation experiments of this study was set above the pressure determined in the experiments designed to delineate the fragmentation threshold in order to ensure full fragmentation and complete ejection. As noted above, the fragmentation threshold of WI21 and WI22 follows the well-defined trend of fragmentation threshold and porosity (Fig. 8), and plots slightly below the fragmentation criterion postulated by Koyaguchi et al. (2008) based on experiments with pristine volcanic rocks from Spieler et al. (2004), Kennedy et al. (2005) and Scheu et al. (2006). The microstructure of these altered ash tuffs is characterized by shards and fragments, cemented mainly by alunite and opal-A (Fig. 3; Heap et al., 2015). This complex microstructure containing altered particles bound by secondary precipitated minerals exhibits a slightly lower tensile strength than that of pristine volcanic rocks and subsequently, fragment slightly below the classically defined fragmentation threshold of Spieler et al. (2004), still obeying the fragmentation criterion.

6.2. Fragmentation and ejection speed

The fragmentation and ejection speed obtained in the experiments are controlled by the initial overpressure within the pores, the connected porosity, the permeability, and the strength of the sample (Scheu et al., 2006; Richard et al., 2013). Here, we clearly demonstrate that, in addition, the state of the decompressing fluid is an important control. Both, the fragmentation and ejection speed increase significantly for those samples fragmented in the presence of steam flashing. The connected porosity allows us to quantify the amount of gas or superheated water stored within the sample. Indeed, Scheu et al. (2006) demonstrated that fragmentation speed is highly influenced by porosity using fragmentation experiments on samples containing different porosities. They showed that fragmentation speeds of 20 and 43 m/s respectively were achieved, when fragmenting samples with 33 and 54% porosities at an initial pressure differential of 10 MPa. These results, for the case of fragmentation by pure argon gas expansion are similar to those for dry argon experiments with WI21 and WI22 in this study. In contrast, during the decompression from 6.5 MPa to ambient pressure, the isothermal expansion of water within the pores and the instantaneous flashing to steam causes a 30-fold larger volume increase compared with pure argon gas expansion under these conditions. Thereby, this process is significantly more violent and energetic (Wohletz, 1983) leading to a faster fragmentation of the sample (as shown in Fig. 9A). As the fragmentation process controls the velocity of the gas–particle mixture (Alatorre-Ibargüengoitia et al., 2011), the ejection speed of the particle front increases with an increase in the fragmentation speed. Therefore, the ejection speed increases with porosity and is significantly higher during steam flashing than for simple gas expansion.

During decompression, the potential energy of gas trapped in pores is converted into kinetic energy as gas expands (Aldibirov and Dingwell, 2000). In this process, part of the energy is consumed by fragmentation and the remaining kinetic energy is left to expel the fragments (Alatorre-Ibargüengoitia et al., 2010). During steam flashing experiments, the scenario is slightly modified as a change in phase is additionally responsible for the gas volume increase powering the fragmentation and ejection processes; yet, the balance in energy used by fragmentation and particle expulsion remains.

In the experiments with loose ash/lapilli (WI27), a grain size reduction was observed which is assumed to be caused by fragmentation, fracturing, and/or comminution. As a consequence of only very minor energy consumed by fragmentation, a higher amount of energy is available for the main energy sinks: namely, the lofting, acceleration, and ejection of the particles. This leads to faster unloading speeds for unconsolidated WI27 compared with the fragmentation speeds of WI22, even though these two samples exhibit similar values of connected porosity. Further, the surplus energy also leads to higher ejection speeds of the particle front for the unconsolidated WI27 samples compared with the cemented WI21 and WI22 samples for both dry and steam flashing experiments (Fig. 9B). Alatorre-Ibargüengoitia et al. (2011) observed that the ejection velocity of the gas–particle mixture is higher than the fragmentation speed of rock samples fragmented by gas expansion. Our results for the ash tuff experiments are in agreement with this observation. We note that the ejection speed of particles in the presence of steam flashing may even be still faster than we report here as the

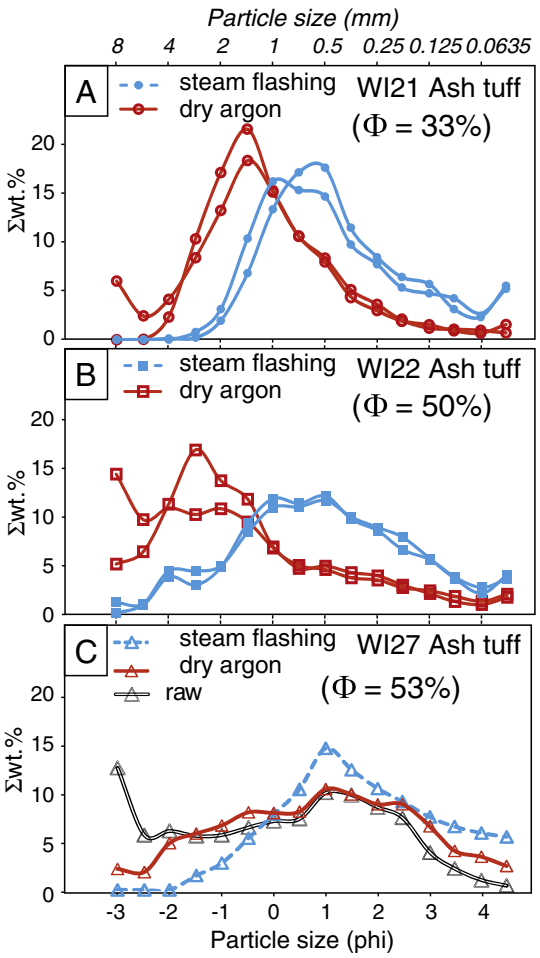

Fig. 11. Particle size distribution plots showing the relation of weight percentage and particle size (phi, phi = $-\log_2 d$, with d = particle diameter in mm) of rapid decompression experiments at 270 °C and 6.5 MPa. Fragmentation of ash tuffs with (A) 33% porosity and (B) 50% porosity as well as ash/lapilli (rrrr) with 53% porosity due to dry argon gas expansion and in the presence of steam flashing. The grain size is decreasing to the right in all three plots, showing a shift to more fines with increasing porosity and a significant shift for fragmentation in the presence of steam flashing. For the unconsolidated ash/lapilli, the grain size distribution prior experimentation (raw) is also plotted. (Note: Given porosities (Φ) refer to average values of experiments shown in the figure and might therefore deviate from average values given in Table 3.).

highest speeds might not have been estimated due to poor visibility during initial phase of ejection of the fastest particles.

The experiments with loose material (WI27) showed that the ejection speed of the first trackable particles is higher than the ejection speed of the ash tuffs but lower than the unloading speeds. In addition, the unloading of the ash/lapilli (in both dry argon and steam flashing experiments) is faster than the ejection speed of particles front.

6.3. Particle size

The production of fine particles in the experiments quantified by the particle size distributions of all fragmented samples is in agreement with the trend identified by Kueppers et al. (2006): an increased production of fine particles results from higher fragmentation energy as a consequence of higher gas volume stored in high porosity samples. Our work shows that a similar effect is induced by steam flashing as the gas volume increases significantly during the phase change. The results support previous assumptions by Wohletz (1983) and Cronin et al. (2003) that steam flashing reduces the particle size in natural eruptions and in shock-tube experiments (e.g., Foote et al., 2011; Rager et al., 2013). Rager et al. (2013) investigated the effect of steam flashing on

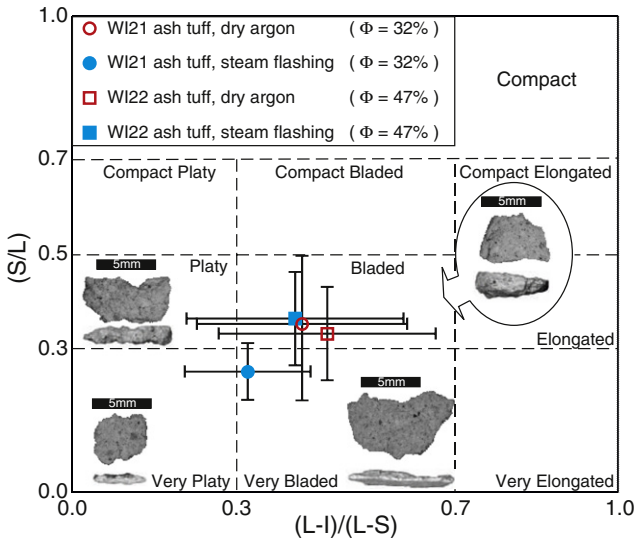

Fig. 12. Particle shape of ash tuffs fragmented by argon gas expansion and in the presence of steam flashing plotted within grain shape fields developed by Sneed and Folk (1958). The grain shape was determined for particles ranging from $-2.5 >$ phi > -1.5 ($5.6 >$ phi > 28 mm). Photomicrographs of particles showing the long versus intermediate and long versus small axes are additionally presented as a reference for all shape fields occupied by investigated ash tuff particles. (Note: Error bars indicate the standard deviation of the measurements. Given porosity values (Φ) are averaged on the samples investigated for the grain shape and might therefore deviate from the values given in Table 3.).

the production of fine particles during the fragmentation of sandstones with an average connected porosity of 27%. The grain size distribution of saturated sandstone fragmented at 300 °C and 15 MPa showed a clear increase in the production of fine particles compared with the control samples fragmented by pure gas expansion.

Particle size analysis prior to and postfragmentation showed that fragmentation processes also occur in experiments with loose samples (WI27) (Fig. 11C). The few coarse particles responsible for the peak in the particle size distribution plot (phi = −3) fragmented during decompression as they could not be observed in the high speed camera recordings. In addition, the peaks in the particle size plot of fragmented ash tuffs (WI21 and WI22) (Fig. 11A, B) are not predetermined by the initial particle sizes of the shards and fragments which are cemented by alunite and opal-A (Fig. 4). In fact, there seems to be no correlation between the dominant particle size of the original clastic rock and the dominant size of fragments. Indeed, most particles generated by fragmentation are aggregates of several cemented particles (Fig. 12).

6.4. Particle shape analysis

The shape analysis of investigated particles showed that for the Whakaari ash tuffs neither sample type nor fragmentation fluid state has a significant influence on the shape (i.e., they plot within the same shape fields; Fig. 12). Here, fragmentation both with and without steam flashing involves fracturing parallel to the decompression front and generate particles with platy or bladed shapes consistent with previous experimental studies (Rager et al., 2013). Although the mean shape of the WI21 particles generated by steam flashing plots within the field of very bladed particles, no significant difference (considering the standard deviation) exists within the investigated particles. Our grain shape analysis results slightly contrast with the findings by Rager et al. (2013) who investigated the shape of volcaniclastic sandstone particles produced by fragmentation experiments with a different degree of sample saturation at 177 °C and 300 °C, respectively. Their study showed that, according to the (S/L) and (L–I)/(L–S) ratio, particles generated by fragmentation at 15 MPa are characterized by a bladed shape and plot within or close to the "bladed" field. However, they showed that full sample saturation (steam flashing) caused a change

of the particle shape in comparison with partial sample saturation, as it leads to the generation of compact bladed particles. This effect is not supported by the analysis of Whakaari ash tuff particles that were fragmented at 6.5 MPa.

We speculate that the shape could be controlled by the initial pressure as well as sample microstructure and inhomogeneity. As a result, we exercise caution here on the subject of using the shape of particles to distinguish between phreatic or gas blast eruptions. Further studies are needed to shed more light on this complex relation.

6.5. Eruption scenarios

Due to its active hydrothermal system, Whakaari's subsurface is characterized by intense fluid migration, storage, and emission. Hydrothermal fluids exist in both liquid and gaseous states within the hydrothermal system at Whakaari and our results have implications for both types of eruption (liquid and gaseous).

In both eruption scenarios, we envisage pressurization of the hydrothermal system to occur if the volume of the uprising fluid supply exceeds the volume of fluids emitted at the surface. One of the main controlling factors here is the permeability of the rocks within the hydrothermal system. Our permeability data (Table 3) highlights that the rocks comprising the hydrothermal system at Whakaari can vary by at least two orders of magnitude. This difference in permeability is likely related to the differences in rock microstructure (Figs. 3 and 4): WI21 is less porous and contains a higher amount of secondary minerals precipitated within the pores (Fig. 4). Hydrothermal sealing has been discussed in several studies (Edmonds et al., 2003; Christenson et al., 2010; Vignaroli et al., 2014; Wyering et al., 2014). Sealing occurs by the deposition of silica and other hydrothermal minerals within the pore and fracture network. Such precipitation is likely to reduce the porosity and permeability of the deposits and will eventually lead to the pressurization of the hydrothermal system. Likewise, dissolution during hydrothermal alteration can increase the permeability of rocks (Wyering et al., 2014).

Eruptions, with or without steam flashing, occur when the pore pressure exceeds the combination of lithostatic and hydrostatic pressure plus the tensile strength of the surrounding rock (Browne and Lawless, 2001). Several triggers may cause the breaking of a mineralogical seal and lead to decompression and hence the expansion of fluids leading to an eruption (Fig. 13).

Here we will focus on the events following full fragmentation and ejection of the sample (i.e. after the decompression of the fluid within the pore network). In the case of gaseous fluids, the expansion and therefore the explosivity of an eruption is less violent than for steam flashing of fluids that are initially liquid and change to a gaseous phase during decompression. Thermodynamics dictate that water at 270 °C and 6.5 MPa will increase in volume 30 times when changing phase into a gas at atmospheric pressure. This volume increase due to the phase transition of water is the crucial reason for the differences in the fragmentation and ejection dynamics of the investigated experiments. Steam flashing causes higher fragmentation speeds, higher ejection speeds and an increased production of fine particles. The hazard potential of such eruptions is therefore much greater than that of gas eruptions, in terms of energy, trajectory distances of ballistics, and size of the area affected by ejecta. Large amounts of very fine particles in a plume represent a persistent, long-lived hazard for the surrounding area. Moreover, eruptions at Whakaari are likely to involve high amounts of unconsolidated material (Fig. 2B). As our results showed, the ash/lapilli (WI27) was ejected at higher speeds and, thus, the probability of ejecta reaching greater distances and spreading over wider areas is increased. Steam flashing phreatic eruptions, which may prove to be the least predictable of all eruptions, are apparently also those containing the highest specific energies for fragmentation and its consequences not only at Whakaari but also at any other hydrothermal system worldwide.

7. Summary and conclusions

We conducted rapid decompression experiments on hydrothermally altered samples (ash tuffs and unconsolidated ash/lapilli) from Whakaari. The experiments, designed to mimic phreatic eruptions, explore the effect of different fluids (dry argon gas versus superheated liquid water) on the fragmentation behavior. The initial conditions were set at 270 °C and 6.5 MPa; rapid decompression to atmospheric pressure triggered fluid expansion, fragmentation and ejection of

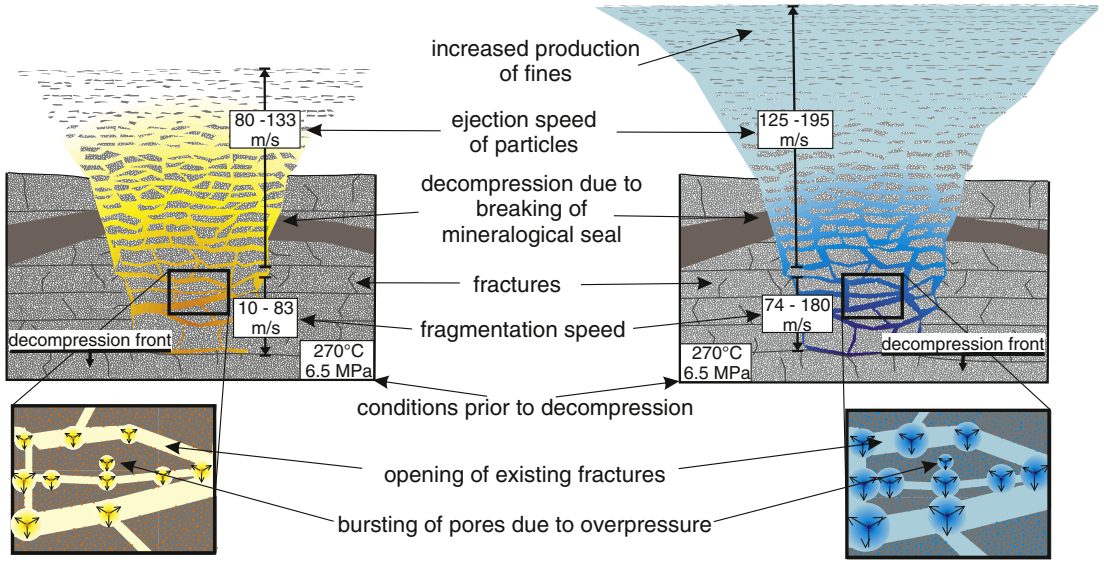

Fig. 13. Schematic model of eruptions driven by gas expansion (left) and steam flashing of liquid water (right). A mineralogical seal allows pressurization of the system; breaking this seal triggers the eruption and leads to a sudden pressure drop. The expansion of gas or liquid water flashing to steam within the pore and fracture network is fragmenting and ejecting the rocks. Initiated at identical pressure and temperature condition the two processes cause differences in the explosivity and therefore violence of the eruption manifested in significantly higher fragmentation and ejection speeds, as well as higher amounts of fines in the presence of steam flashing.

particles. Our results show the influence of argon expansion versus steam flashing as well as sample type and secondary hydrothermal alteration (among others alunite precipitation) on the fragmentation threshold and speed as well as the particle size, shape and ejection velocities.

(1) The rapid decompression experiments revealed that fragmentation and ejection speeds of two ash tuffs, cemented by alunite and amorphous opal, increase with increasing porosity and that both are significantly enhanced in the presence of steam flashing.
(2) The energy consumption by fragmentation leads to reduced ejection speeds of cemented tuffs in comparison with unconsolidated samples.
(3) Fragmentation dominated by steam flashing also results in increased fragmentation energy and increased proportion of fine particles.
(4) For the investigated Whakaari samples the phase of the fluid just prior to fragmentation showed no significant influence on the particle shape as revealed by analysis before and after fragmentation. Both steam flashing and pure gas expansion produce platy or bladed particles from fracturing parallel to the decompression front.

In summary, under identical pressure and temperature conditions, eruptions accompanied by the process of liquid water flashing to steam are significantly more violent than those driven simply by gas expansion. Phase changes during decompression together with the type and amount of cementation are important fragmentation variables and should therefore be considered for hazard assessment and modeling of eruptions in hydrothermally active environments.

Acknowledgments

This project has received funding from the European Union's Seventh Programme for research, technological development, and demonstration under grant agreement no. 282759 (VUELCO). M. J. Heap and B. Scheu acknowledge the support of a PROCOPE grant (Hot Hydrothermal Volcanic Systems; project-ID 57130387), funded and implemented by the Deutscher Akademischer Austauschdienst (DAAD) in Germany, and the Ministry of Foreign and European Affairs (MAE) and the Ministry of Higher Education and Research (MESR) in France. M. J. Heap and B. M. Kennedy acknowledge a Hubert Curien Partnership (PHC) Dumont d'Urville Grant (grant number 31950RK), funded and implemented by the New Zealand Ministry of Business, Innovation and Employment (MBIE) and the Royal Society of New Zealand in New Zealand, and the Ministry of Foreign Affairs (MAEDI) and the Ministry of Higher Education and Research (MENESR) in France. M. J. Heap also acknowledges J. I. Farquharson for his role in the reconstruction of the benchtop permeameter at EOST Strasbourg. D.B. Dingwell acknowledges the support of the ERC Advanced Investigator Grant (EVOKES — no. 247076). The authors wish to thank Thierry Reuschlé for the permeability measurement of WI27 at EOST Strasbourg. Furthermore the authors acknowledge Cristian Montanaro for help while performing the fragmentation experiments and for his helpful comments. Field access was provided by the Buttle Family, Pee Jay Tours, and the New Zealand Royal Air Force, in conjunction with GNS Science. This manuscript benefitted from constructive comments of an anonymous reviewer and the editor Margaret T. Mangan.

Appendix A. Supplementary data

Supplementary data to this article can be found online at http://dx.doi.org/10.1016/j.jvolgeores.2015.06.014.

References

Alatorre-Ibargüengoitia, M.A., Scheu, B., Dingwell, D.B., Delgado-Granados, H., Taddeucci, J., 2010. Energy consumption by magmatic fragmentation and pyroclast ejection during Vulcanian eruptions. Earth Planet. Sci. Lett. 291 (1), 60–69.
Alatorre-Ibargüengoitia, M.A., Scheu, B., Dingwell, D.B., 2011. Influence of the fragmentation process on the dynamics of Vulcanian eruptions: an experimental approach. Earth Planet. Sci. Lett. 302 (1), 51–59.
Alidibirov, M., Dingwell, D.B., 1996a. An experimental facility for the investigation of magma fragmentation by rapid decompression. Bull. Volcanol. 58 (5), 411–416.
Alidibirov, M., Dingwell, D.B., 1996b. Magma fragmentation by rapid decompression. Nature 380 (6570), 146–148.
Alidibirov, M., Dingwell, D.B., 2000. Three fragmentation mechanisms for highly viscous magma under rapid decompression. J. Volcanol. Geotherm. Res. 100 (1), 413–421.
Bartrum, J.A., 1926. White Island Volcano. N. Z. J. Sci. Technol. 8 (5), 261–266.
Bergmann, J., Friedel, P., Kleeberg, R., 1998. BGMN—a new fundamental parameters based Rietveld program for laboratory X-ray sources, its use in quantitative analysis and structure investigations. CPD Newsl. 20, 5–8.
Black, P.M., 1970. Observations on White Island volcano, New Zealand. Bull. Volcanol. 34 (1), 158–167.
Bloomberg, S., Werner, C., Rissmann, C., Mazot, A., Horton, T., Gravley, D., Kennedy, B., Oze, C., 2014. Soil CO_2 emissions as a proxy for heat and mass flow assessment, Taupō Volcanic Zone, New Zealand. Geochem. Geophys. Geosyst. 15 (12), 4885–4904 (ISO 690).
Breard, E.C.P., Lube, G., Cronin, S.J., Fitzgerald, R., Kennedy, B., Scheu, B., Montanaro, C., White, J.D.L., Tost, M., Procter, J.N., Moebis, A., 2014. Using the spatial distribution and lithology of ballistic blocks to interpret eruption sequence and dynamics: August 6, 2012 Upper Te Maari eruption, New Zealand. J. Volcanol. Geotherm. Res. 286, 373–386.
Browne, P., Lawless, J., 2001. Characteristics of hydrothermal eruptions, with examples from New Zealand and elsewhere. Earth Sci. Rev. 52, 229–331.
Buttinelli, M., De Rita, D., Cremisini, C., Cimarelli, C., 2011. Deep explosive focal depths during maar forming magmatic-hydrothermal eruption: Baccano Crater, Central Italy. Bull. Volcanol. 73 (7), 899–915.
Chardot, L., Jolly, A.D., Kennedy, B., Fournier, N., Sherburn, S., 2015. Using volcanic tremor for eruption forecasting at White Island volcano (Whakaari), New Zealand. J. Volcanol. Geotherm. Res. 302, 11–23.
Christenson, B.W., Reyes, A.G., Young, R., Moebis, A., Sherburn, S., Cole-Baker, J., Britten, K., 2010. Cyclic processes and factors leading to phreatic eruption events: Insights from the 25 September 2007 eruption through Ruapehu Crater Lake, New Zealand. J. Volcanol. Geotherm. Res. 191 (1), 15–32.
Christoffel, D. A. (1989). Variations in magnetic field intensity at White Island volcano related to the 1976–82 eruption sequence. In: Houghton, B. F., and Nairn, I. A. (1991). The 1976–1982 strombolian and phreatomagmatic eruptions of White Island, New Zealand: eruptive and depositional mechanisms at a 'wet' volcano. Bulletin of Volcanology, 54(1), 25–49.
Clark, R.H., Otway, P.M., 1982. Deformation monitoring associated with the 1976–82 White Island eruption sequence. In: Houghton, B.F., Nairn, I.A. (Eds.), The 1976–82 Eruption Sequence at White Island Volcano (Whakaari), Bay of Plenty, New Zealand, New Zealand Geological Survey Bulletin 103. New Zealand Geological Survey, Lower Hutt, pp. 69–84.
Cole, J.W., Nairn, I.A., 1975. Catalogue of the active volcanoes and Solfatara fields of New Zealand, part XXII. In: Decker, R.W. (Ed.), Catalogue of the Active Volcanoes of the World Including Solfatara Fields. International Association of Volcanology and Chemistry of the Earth's Interior, Rome, pp. 38–49.
Cole, J.W., Thordarson, T., Burt, R.M., 2000. Magma origin and evolution of White Island (Whakaari) Volcano, Bay of Plenty, New Zealand. J. Petrol. 41 (6), 867–895.
Cronin, S.J., Neall, V.E., Lecointre, J.A., Hedley, M.J., Loganathan, P., 2003. Environmental hazards of fluoride in volcanic ash: a case study from Ruapehu volcano, New Zealand. J. Volcanol. Geotherm. Res. 121 (3), 271–291.
Duncan, A.R., 1970. The Petrology and Petrochemistry of Andesite and Dacite Volcanoes in Eastern Bay of Plenty, New Zealand Ph.D. Thesis Victoria University of Wellington, New Zealand.
Edmonds, M., Oppenheimer, C., Pyle, D.M., Herd, R.A., Thompson, G., 2003. SO_2 emissions from Soufriere Hills Volcano and their relationship to conduit permeability, hydrothermal interaction and degassing regime. J. Volcanol. Geotherm. Res. 124 (1), 23–43.
Fitzgerald, R.H., Tsunematsu, K., Kennedy, B.M., Breard, E.C.P., Lube, G., Wilson, T.M., Jolly, A.D., Pawson, J., Rosenberg, M.D., Cronin, S.J., 2014. The application of a calibrated 3D ballistic trajectory model to ballistic hazard assessments at Upper Te Maari Tongariro. J. Volcanol. Geotherm. Res. 286, 248–262.
Foote, L.C., Scheu, B., Kennedy, B., Gravley, D., Dingwell, D.B., 2011. Experimental calibration of phreatic and hydrothermal explosions: a case study on lake Okaro, New Zealand. New Zealand Geothermal Workshop 2011 Proceedings.
Fournier, N., Chardot, L., 2012. Understanding volcano hydrothermal unrest from geodetic observations: Insights from numerical modeling and application to White Island volcano, New Zealand. J. Geophys. Res. Solid Earth (1978–2012) 117 (B11).
Fowler, A.C., Scheu, B., Lee, W.T., McGuinness, M.J., 2010. A theoretical model of the explosive fragmentation of vesicular magma. Proc. R. Soc. A: Math. Phys. Eng. Sci. 466 (2115), 731–752 (The Royal Society).
Giggenbach, W.F., 1987. Redox processes governing the chemistry of fumarolic gas discharges from White Island, New Zealand. Appl. Geochem. 2 (2), 143–161.
Giggenbach, W.F., Glasby, C.P., 1977. Influence of thermal activity on the trace metal distribution in marine sediments around White Island, New Zealand. N. Z. Dep. Sci. Ind. Res. Bull. 218, 121–126.

Giggenbach, W.F., Shinohara, H., Kusakabe, M., Ohba, T., 2003. Formation of acid volcanic brines through interaction of magmatic gases, seawater and rock within the White Island volcanic–hydrothermal system, New Zealand. Soc. Econ. Geol. Spec. Publ. 10, 19–40.
Global Volcanism Program, 2014. Report on White Island (New Zealand). In: Wunderman, R. (Ed.), Bulletin of the Global Volcanism Network 39. Smithsonian Institution, p. 2.
Graham, I.J., Cole, J.W., 1991. Petrogenesis of andesites and dacites of White Island volcano, Bay of Plenty, New Zealand, in the light of new geochemical and isotopic data. N. Z. J. Geol. Geophys. 34 (3), 303–315.
Hamilton, W.M., Baumgart, I.L., 1959. White Island, Department of Scientific and Industrial Research Bulletin. 127 pp. 9–24.
Heap, M.J., Lavallée, Y., Laumann, A., Hess, K.U., Meredith, P.G., Dingwell, D.B., 2012. How tough is tuff in the event of fire? Geology 40 (4), 311–314.
Heap, M.J., Kennedy, B., Pernin, N., Jacquemard, L., Baud, P., Farquharson, J., Scheu, B., Lavallée, Y., Gilg, H.A., Letham-Brake, M., Mayer, K., Jolly, A., Reuschlé, T., Dingwell, D.B., 2015. Mechanical behavior and failure modes in the Whakaari (White Island volcano) hydrothermal system, New Zealand. J. Volcanol. Geotherm. Res. 295, 26–42.
Houghton, B.F., Nairn, I.A., 1989a. A model for the 1976–82 phreatomagmatic and strombolian eruption sequence at White Island volcano. N. Z. Geol. Surv. Bull. 103, 127–136.
Houghton, B.F., Nairn, I.A., 1989b. The phreatomagmatic and strombolian eruption events at White Island volcano 1976–82: eruption narrative. In: Houghton, B.F., Nairn, I.A. (Eds.), The 1976–82 Eruption Sequence at White Island Volcano (Whakaari), Bay of Plenty, New Zealand. New Zealand Geological Survey Bulletin 103. New Zealand Geological Survey, Lower Hutt, pp. 13–23.
Houghton, B.F., Nairn, I.A., 1991. The 1976–1982 strombolian and phreatomagmatic eruptions of White Island, New Zealand: eruptive and depositional mechanisms at a 'wet' volcano. Bull. Volcanol. 54, 25–49.
Hurst, A.W., Rickerby, P.C., Scott, B.J., Hashimoto, T., 2004. Magnetic field changes on White Island, New Zealand, and the value of magnetic changes for eruption forecasting. J. Volcanol. Geotherm. Res. 136 (1), 53–70.
Hurst, T., Jolly, A.D., Sherburn, S., 2014. Precursory characteristics of the seismicity before the 6 August 2012 eruption of Tongariro volcano, North Island, New Zealand. J. Volcanol. Geotherm. Res. 286, 294–302.
Jolly, A.D., Chardot, L., Neuberg, J., Fournier, N., Scott, B.J., Sherburn, S., 2012. High impact mass drops from helicopter: a new active seismic source method applied in an active volcanic setting. Geophys. Res. Lett. 39 (12), 1–5.
Kennedy, B., Spieler, O., Scheu, B., Kueppers, U., Taddeucci, J., Dingwell, D.B., 2005. Conduit implosion during Vulcanian eruptions. Geology 33 (7), 581–584.
Koyaguchi, T., Scheu, B., Mitani, N.K., Melnik, O., 2008. A fragmentation criterion for highly viscous bubbly magmas estimated from shock tube experiments. J. Volcanol. Geotherm. Res. 178 (1), 58–71.
Kueppers, U., Scheu, B., Spieler, O., Dingwell, D.B., 2006. Fragmentation efficiency of explosive volcanic eruptions: a study of experimentally generated pyroclasts. J. Volcanol. Geotherm. Res. 153 (1), 125–135.
Letham-Brake, M., 2013. Geological constraints on fluid flow at Whakaari volcano (White Island) M.Sc. Thesis, Department of Geological SciencesUniversity of Canterbury, Christchurch, New Zealand (http://ir.canterbury.ac.nz/handle/10092/8728).
Martel, C., Dingwell, D.B., Spieler, O., Pichavant, M., Wilke, M., 2000. Fragmentation of foamed silicic melts: an experimental study. Earth Planet. Sci. Lett. 178 (1), 47–58.
Mastin, L.G., 1995. Thermodynamics of gas and steam-blast eruptions. Bull. Volcanol. 57 (2), 85–98.
Moon, V., Bradshaw, J., Smith, R., de Lange, W., 2005. Geotechnical characterization of stratocone crater wall sequences, White Island volcano, New Zealand. Eng. Geol. 81 (2), 146–178.
Moon, V., Bradshaw, J., de Lange, W., 2009. Geomorphic development of White Island volcano based on slope stability modelling. Eng. Geol. 104 (1), 16–30.
Morgan, L.A., Shanks, W.P., Pierce, K.L., 2009. Hydrothermal processes above the Yellowstone magma chamber: large hydrothermal systems and large hydrothermal explosions. Geol. Soc. Am. Spec. Pap. 459, 1–95.
Mueller, S., Melnik, O., Spieler, O., Scheu, B., Dingwell, D.B., 2005. Permeability and degassing of dome lavas undergoing rapid decompression: an experimental determination. Bull. Volcanol. 67 (6), 526–538.
Mueller, S., Scheu, B., Spieler, O., Dingwell, D.B., 2008. Permeability control on magma fragmentation. Geology 36 (5), 399–402.
Nishi, Y., Sherburn, S., Scott, B.J., Sugihara, M., 1996. High-frequency earthquakes at White Island volcano, New Zealand: insights into the shallow structure of a volcano–hydrothermal system. J. Volcanol. Geotherm. Res. 72 (3), 183–197.
Peltier, A., Scott, B., Hurst, T., 2009. Ground deformation patterns at White Island volcano (New Zealand) between 1967 and 2008 deduced from levelling data. J. Volcanol. Geotherm. Res. 181 (3), 207–218.
Pirajno, F., 2009. Hydrothermal Processes and Mineral Systems. Springer, Netherlands, p. 1250 (http://dx.doi.org/10.1007/978-1-4020-8613-7).
Pola, A., Crosta, G.B., Fusi, N., Castellanza, R., 2013. General characterization of the mechanical behavior of different volcanic rocks with respect to alteration. Eng. Geol. 169, 1–13.
Rager, A.H., Smith, E.I., Scheu, B., Dingwell, D.B., 2013. The effects of water vaporization on rock fragmentation during rapid decompression: implications for the formation of fluidized ejecta on Mars. Earth Planet. Sci. Lett. 385, 68–78.
Richard, D., Scheu, B., Mueller, S.P., Spieler, O., Dingwell, D.B., 2013. Outgassing: influence on speed of magma fragmentation. J. Geophys. Res. Solid Earth 118 (3), 862–877.
Scheu, B., Spieler, O., Dingwell, D.B., 2006. Dynamics of explosive volcanism at Unzen volcano: an experimental contribution. Bull. Volcanol. 69 (2), 175–187.
Scheu, B., Kueppers, U., Mueller, S., Spieler, O., Dingwell, D.B., 2008. Experimental volcanology on eruptive products of Unzen volcano. J. Volcanol. Geotherm. Res. 175 (1), 110–119.
Scheu, B., Serr, F., Dingwell, D.B., 2011. Phreatic and hydrothermal explosions — a lab approach. Geophys. Res. Abstr. 13 (EGU2011-1669).
Sherburn, S., Scott, B.J., Nishi, Y., Sugihara, M., 1998. Seismicity at White Island volcano, New Zealand: a revised classification and inferences about source mechanism. J. Volcanol. Geotherm. Res. 83 (3), 287–312.
Simkin, T., Siebert, L., 1994. Volcanoes of the World: A Regional Directory, Gazetteer, and Chronology of Volcanism During the Last 10,000 Years. Geoscience, Press, Inc., Tucson, Arizona, p. 349 (in association with the Smithsonian Institute).
Sneed, E.D., Folk, R.L., 1958. Pebbles in the lower Colorado River, Texas a study in particle morphogenesis. J. Geol. 66, 114–150.
Spieler, O., Alidibirov, M., Dingwell, D.B., 2003. Grain-size characteristics of experimental pyroclasts of 1980 Mount St. Helens cryptodome dacite: effects of pressure drop and temperature. Bull. Volcanol. 65 (2–3), 90–104.
Spieler, O., Kennedy, B., Kueppers, U., Dingwell, D.B., Scheu, B., Taddeucci, J., 2004. The fragmentation threshold of pyroclastic rocks. Earth Planet. Sci. Lett. 226 (1), 139–148.
Vignaroli, G., Aldega, L., Balsamo, F., Billi, A., De Benedetti, A.A., De Filippis, L., Giordano, G., Rossetti, F., 2014. A way to hydrothermal paroxysm, Colli Albani volcano, Italy. Geological Society of America Bulletin http://dx.doi.org/10.1130/B31139.1 (B31139-1).
Ward, G.A., 1922. White Island. N. Z. J. Sci. Technol. 5, 220–226.
Werner, C., Hurst, T., Scott, B., Sherburn, S., Christenson, B.W., Britten, K., Cole-Baker, J., Mullan, B., 2008. Variability of passive gas emissions, seismicity, and deformation during crater lake growth at White Island volcano, New Zealand, 2002–2006. J. Geophys. Res. Solid Earth (1978–2012) 113 (B1).
Wohletz, K.H., 1983. Mechanisms of hydrovolcanic pyroclast formation: grain-size, scanning electron microscopy, and experimental studies. J. Volcanol. Geotherm. Res. 17 (1), 31–63.
Wood, C.P., Browne, P.R., 1996. Chlorine-rich pyrometamorphic magma at White Island volcano, New Zealand. J. Volcanol. Geotherm. Res. 72 (1), 21–35.
Wyering, L.D., Villeneuve, M.C., Wallis, I.C., Siratovich, P.A., Kennedy, B.M., Gravley, D.M., Cant, J.L., 2014. Mechanical and physical properties of hydrothermally altered rocks, Taupo Volcanic Zone, New Zealand. J. Volcanol. Geotherm. Res. 288, 76–93.
Zimanowski, B., Fröhlich, G., Lorenz, V., 1991. Quantitative experiments on phreatomagmatic explosions. J. Volcanol. Geotherm. Res. 48 (3), 341–358.

Further reading

Clark, R.H., Cole, J.W., 1989. Volcanic monitoring and surveillance at White Island before the 1976–82 eruption sequence. In: Houghton, B.F., Nairn, I.A. (Eds.), The 1976–82 Eruption Sequence at White Island volcano (Whakaari), Bay of Plenty, New Zealand. New Zealand Geological Survey Bulletin 103. New Zealand Geological Survey, Lower Hutt, pp. 13–23.
Smithsonian Institution, 2013. White Island. Volcanoes of the World 4.0: The volcano and eruption database of Smithsonian's Global Volcanism Program Retrieved 2 Oct. 2013 from:http://www.volcano.si.edu/volcano.cfm?vn=241040.